Research Square

Preprints are preliminary reports that have not undergone peer review.
They should not be considered conclusive, used to inform clinical practice,
or referenced by the media as validated information.

Tunable multifunctionality in aliovalent substituted Bi12MnO20 sillenite for thermistor and other fascinating applications

Harshavardhan Chouhan
Central Institute of Technology, Kokrajhar
Upasana Basumatary
Kokrajhar University (Erstwhile Kokrajhar Govt. College), Kokrajhar
Rimpi Chakravarty
Indian Institute of Technology Guwahati
Mahanta Chouhan
Central Institute of Technology, Kokrajhar
R. K. Parida
Siksha O Anusandhan University
B. N. Parida
Central Institute of Technology, Kokrajhar
S. Bhattacharjee
sourav@kokrajharuniversity.ac.in

Kokrajhar University (Erstwhile Kokrajhar Govt. College), Kokrajhar https://orcid.org/0000-0003-0484-1555

Research Article

Keywords: Sillenite oxide, Thermistor, UV-Visible, Weak Ferromagnetism

Posted Date: March 5th, 2026

DOI: https://doi.org/10.21203/rs.3.rs-9030792/v1

License: This work is licensed under a Creative Commons Attribution 4.0 International License.
Read Full License

Additional Declarations:
The authors declare no competing interests.

Table 1 to 3 are available in the Supplementary Files section.

Tunable multifunctionality in aliovalent substituted $Bi_{12}MnO_{20}$ sillenite for thermistor and other fascinating applications

[2]Harshavardhan Chouhan, [1]Upasana Basumatary, [4]Rimpi Chakravarty, [2]Mahanta Chouhan, [3]R. K. Parida, [2]B. N. Parida and [1]S. Bhattacharjee*

[1]Department of Physics, Kokrajhar University (Erstwhile Kokrajhar Govt. College), Kokrajhar, BTR, Assam, India-783370

[2]Department of Physics, Central Institute of Technology, Kokrajhar (Deemed to be University, MoE, Govt. of India), BTR, Assam, India-783370

[3]Department of Physics, Siksha O Anusandhan University (Deemed to be University), Khandigiri, Bhubaneswar, India-751030

[4]Department of Physics, Indian Institute of Technology Guwahati, Assam, India-781039

Abstract

A new aliovalent-substituted $Bi_{12}MnO_{20}$ sillenite is synthesized incorporating solid-state reaction route at optimized temperature 800°C. Structural analysis through Fullprof Rietveld refinement of XRD data confirmed a cubic *I*23 structure with lattice and reliability parameters a = 10.105 Å and (R_p = 9.05%, R_{wp} = 15.95%, R_{exp} = 12.11% and χ^2 = 1.74) respectively. The Williamson-Hall analysis indicated 1.344 nm crystallites and 0.0162 strain. The microstructural analysis through SEM displayed polycrystalline morphology with blocky, agglomerated grains with average grain size 255 nm. The color mapping of EDX spectra verified the expected elements in the system. The FTIR analysis gives the blueprint of sillenite vibrations in the wave number range 400–600 cm^{-1}. UV-Vis spectroscopy revealed strong 317 nm absorbance and a 2.31 eV direct bandgap in the synthesized sample. Dielectric responses followed the Maxwell-Wagner model, with temperature-activated polaron hopping, non-Debye relaxation, NTCR feature, and multi-interface contributions evident in Impedance/Modulus spectra. Conductivity adhered to Jonscher's power law, enhanced by aliovalent substitution with Mn at tetrahedral site. I-V characteristics confirmed n-type semiconducting behavior, with a thermistor coefficient β = 4157.3 K obtained through fitting Steinhart-Hart equation. Magnetic analysis features weak ferromagnetism with M_R = 0.005 emu/g, H_c = 115.84 Oe and M_s = 0.839 emu/g obtained via Grosinger's LAS model. These properties highlight potential of the synthesized sillenite material in UV photocatalytic, thermistors and magneto-electric devices oriented applications.

Keywords: Sillenite oxide; Thermistor; UV-Visible; Weak Ferromagnetism

*Corresponding Author: sourav@kokrajharuniversity.ac.in

Introduction

Sillenites are a distinct class of bismuth-based compounds with the general stiochiometric formula $Bi_{12}MO_{20}$, where *M* represents generally a tetravalent cation or a combination of cations averaging a +4 oxidation state, such as Si^{4+}, Ge^{4+}, or mixed-valent pairs like Fe^{3+} and P^{5+}. These compounds are structurally related to the metastable γ-phase of bismuth oxide (Bi_2O_3), which adopts a body-centered cubic (bcc) structure with space group *I23*. This phase, originally unstable in pure Bi_2O_3, can be stabilized through the incorporation of small quantities of dopant cations, leading to the formation of sillenite-type structures [1]. The sillenite crystal structure is characterized by a complex three-dimensional framework composed of Bi–O polyhedra and MO_4 tetrahedra. Bismuth ions occupy the A-sites of the lattice and are coordinated with five oxygen atoms and a stereochemically active $6s^2$ lone pair, forming distorted BiO_5 polyhedra. These units connect to regular MO_4 tetrahedra, where the M-site cation resides at the center of a four-oxygen tetrahedron [2]. This interconnected network gives rise to a pseudo-body-centered cubic unit cell, with the structure belonging to the non-centrosymmetric space group *I23* (No. 197) [3]. As a result, sillenites can exhibit piezoelectric behavior, although they are not ferroelectric due to the lack of a permanent dipole [2,4–6]. In addition to their stoichiometric forms, sillenites allow for a range of non-stoichiometric compositions through aliovalent substitution at the M-site. Such substitutions can create oxygen vacancies or interstitials, and charge neutrality is maintained by adjusting the average valence state of the M-site cations. For instance, compositions like $Bi_{12}(Bi_{0.03}V_{0.89}X_{0.08})O_{20.27}$ and $Bi_{12}(Bi_{0.5}Ga_{0.5})O_{19.5}$ exemplify this flexibility . The ability of the sillenite framework to accommodate diverse chemical species and structural distortions makes these materials of considerable interest for applications in various sectors. These compounds exhibit a wide range of intriguing physical properties, making them highly attractive for advanced technological applications. These materials function as semi-insulating yet photoconductive, photoluminescent, electro-optic, magneto-optic, acousto-optic, optically active and piezoelectric systems because of their large band gaps and high resistivity. They are hence good candidates for application in optoelectronics, photonics, and optical information

processing because to their exceptional photorefractive and photochromatic characteristics [3,7–11]. M. Isik et. al [5] using DFT calculations stated that $Bi_{12}SiO_{20}$ with a broad bandgap of about 3.2 eV might be used for photo-catalysis and photo-transducer-oriented applications. While stoichiometric sillenites, such as $Bi_{12}MO_{20}$ (where M = Si, Ge, or Ti), have long been recognised for their electro-optic behaviour, attention has recently shifted to their dielectric properties, particularly for applications involving low-temperature cofired ceramics (LTCC). These materials offer advantages such as low sintering temperatures (typically ≤ 850 °C), compatibility with silver electrodes, low dielectric loss, and a stable permittivity ($\varepsilon_r \approx 35–40$) near room temperature [11]. Despite these promising traits, limited studies have investigated their dielectric responses across various temperatures and frequencies, with some reports, like that of $Bi_{12}(B_{0.5}P_{0.5})O_{20}$, revealing broad, relaxor-like anomalies due to cation disorder. Yu Hu et. al [11] also claimed in their work non-ferroelectric relaxor like feature in $Bi_{12}SiO_{20}$ arise due to chaotic local dipole moment link with polyhedron network BiO_5 via $6S^2$ lone pair. Matjaz Valent et. al claimed in their investigation on non-stiochiomatic sillenites $Bi_{12}XO_{20-\gamma}$ (where X = Ti, Ge, Si, Mn, $B_{0.5}P_{0.5}$) at microwave frequency range that $Bi_{12}SiO_{20}$ is potentially active candidate for LTCC applications [12].

Based on the fascinating spectra illustrated by sillenites compound, in this work we have focus primarily on dielectric, electric and optical feature of a new multication oriented sillenite $Bi_{12}Mn_{0.5}Fe_{0.25}Ni_{0.25}O_{20-\delta}$ with the expectation that the aliovalent substituents Fe and Ni at M site with Mn disturbed the local symmetry through the creation of defect/oxygen vacancy, which influence the dielectric and associate property of the investigated sillenite material.

Experimental Techniques:

The new aliovalent substituted sillenite based compound, namely $Bi_{12}Mn_{0.5}Fe_{0.25}Ni_{0.25}O_{20-\delta}$ was synthesized through a standard solid oxide route process. High-purity analytical reagent-grade oxides (around 99.99% purity) supplied by Loba Chem. Pvt. Ltd. were employed, namely Bi_2O_3, MnO_2, Fe_2O_3 & Ni_2O_3. The proportions of these raw materials were calculated based on a general stoichiometric equation as shown below to obtain the desired composition.

$$6\ Bi_2O_3 + 0.5\ MnO_2 + 0.125\ Fe_2O_3 + 0.125\ Ni_2O_3 \text{-------}\rightarrow Bi_{12}Mn_{0.5}Fe_{0.25}Ni_{0.25}O_{20-\delta}$$

The required amounts of these precursors were precisely weighed using a digital balance with an accuracy of up to three decimal places. Afterwards, the mixture was manually ground in air for approximately 1-2 hours, followed by wet grinding with methanol until thoroughly dried, utilizing a mortar pestle set. The homogenized mixture was transferred into a clean crucible of alumina and heated using a programmable high-temperature furnace under controlled conditions in a sequential manner. After completion of calcinations process at 800^0C, the product was collected as a dense mass and reground into fine powder.

To explore the crystallinity and phase purity, the calcined sample was analyzed using an X-ray diffractometer (Rigaku model) and Fullprof Reitveld refinement software within the specific diffraction angle range 20^0-80^0. Further conformation of sillenite phase and involvements of various modes of vibrations were identified through Shimadzu: IRAffinity -1S FTIR spectrometer. UV–Visible absorption measurements were performed using a Shimadzu 2600 spectrometer to determine optical response and estimate the energy band gap. For dielectric/impedance characterizations, part of the processed powder was pressed into cylindrical pellet (≈10 mm diameter and 1.5 mm thickness) using PVA as a binder and a pressing machine.

The pellet was then sintered at around 850^0C for five hours to achieve densification and complete removal of the binder. Before conducting the dielectric or conductivity tests, both sides of the pellet was coated with high-purity silver adhesive, followed by oven drying at 100^0C for around 1 hour. The dielectric features were then examined using an impedance analyzer meter in the frequency range of (0.1 to 5000) kHz, over wide range of temperature. The leakage current (I-V characteristics) was measured using a Keithley electrometer from 25^0C – 300^0C. Magnetic properties were further examined employing a vibrating sample magnetometer (VSM) to assess magnetic order/disorder phenomena at ambient conditions. The morphological and compositional spectra of the powder sample were carried out at ambient condition through ZEISS Gemini 300 model equipped with OXFORD EDX meter.

Structure Analysis:

The Fullprof Reitveld analysis of experimental XRD data of the synthesized sample (as depicted in Fig.1(a)) confirmed the formation of new sillenite structure namely

$Bi_{12}Mn_{0.5}Fe_{0.25}Ni_{0.25}O_{20-\delta}$ with usual cubic symmetry (space group = *I*23) and lattice parameters 'a' = 'b' = 'c' = 10.105 Å. Besides one impurity phase namely Fe_2O_3 is identified with structural symmetry cubic (space group = Fd3m) and lattice parameters 'a' = 'b' = 'c' = 8.33 Å. The percentage contribution of phase 1 (Sillenite) and that of phase 2 (Fe_2O_3) in the synthesized sample is found to be 86.85 % and 13.15 % respectively. The information of Bragg's planes and Bragg's angles obtained for both the phases for the synthesized sample is illustrated in Table 1. The detailed atomic positions along with the cell parameters obtained through refinement for both the phases and also the schematic structural configuration developed through VESTA software is illustrated in Table 2 and Fig. 1 (b) respectively. The value of the reliability parameters and $(chi)^2$, that is, R_P (%) = 9.05, R_{WP} (%) = 15.95, R_{exp} (%) = 12.11, χ^2 = 1.74 , obtained through Reitveld refinement clarifies the goodness of fit as well as the great resemblance between the experimental and fitted data.

To extract the information of crystallize size and lattice strain in the synthesized sample, the XRD data is fitted through Williamson-Hall equation $\boldsymbol{\beta\, Cos\theta = 4\, \varepsilon\, Sin\theta + k\, \lambda/D}$ [13] (where β = Full width at half maximum, θ = Bragg's angle, ε = Lattice strain, λ = Wavelength of incident X-Ray = 1.5406 Å & D = crystallize size) as illustrated in Fig. 1 (c). Based on the goodness of fit, the value of crystallize size and lattice strain is estimated to be 1.344 nm and 0.0162 respectively.

SEM & EDX spectroscopy:

The morphology of the investigated sillenite sample analyzed through scanning electron microscopy (SEM) at room temperature (as depicted in Fig. 2 (a)) clarify the polycrystalline nature of the sample filled with agglomerated grains, minimal intergranular space and blocky morphology. Besides, the appearance of mixed shape grains indicates the different grain growth rate governed by anisotropic surface energy in the sample. The dimension of the grains is found to lie in the range 100-1200 nm with average grain size estimated through fitting a Gaussian distribution curve on the histogram plot (as shown in Fig. 2 (b)) is 255.06 nm. In many sillenite samples such type of morphology is reported to arise due to high temperature solid route synthesis as well as doping of transition metal ions [12,14].

The compositional analysis carried out through EDX spectroscopy (as shown in Fig. 2 (c)) clarified the involvement of primary raw elements namely Bi, Mn, Fe, Ni and O without any trace of foreign elements in the synthesized sillenite sample. Besides, the color mapping of EDX

spectra (as depicted in Fig. 2 (d)) suggest uniform distribution of the elements throughout the surface without any sort of clustering.

FTIR spectroscopy:

The investigation of various involved modes of vibrations as well as conformation of sillenite phase in the synthesized sample is conducted through FTIR spectroscopic technique. The FTIR spectrum of the inspected sample consists of a wide range of dips extending from (400 - 3744) cm^{-1} as illustrated in Fig. 3. The clustering of peaks appear in the low wave number range (400 - 600) cm^{-1} is a characteristic signature of phonon initiate lattice mode of vibrations arise due to distortion of Bi-O-M (where M = Mn, Fe & Ni) network through the incorporation of transition metal ions Fe & Ni at the tetrahedral site of the sillenite phase [15,16]. The band appears in the range (409 - 447) cm^{-1} assigned to internal Bi-O-Bi stretching and Bi-O bending vibrations in Bi-O polyhedra. The overlapping of O-Bi-O deformation modes with weak M-O bond in the tetrahedron site correspond to the bands in the range (460-478) cm^{-1}. The band appears in the range (484 - 509) cm^{-1} assigned to Bi-O stretching in BiO5 polyhedra. The strong Bi-O-M bending modes of vibration trigger the bands in the range (523-532) cm^{-1}. The dip appears in the range (560 - 594) cm^{-1} are the signature bands of transition metal based sillenites triggered through the vibration of Mn-O/Fe-O/Ni-O bonds at the tetrahedral sites [15]. The band at 1040 cm^{-1} arises due to extended M-O stretching of the distorted BiO_5 polyhedron through the asymmetric substitution of Fe and Ni in the sillenite network. The bands in the range at (1416 - 1800) cm^{-1} are expected to arise due to weak overtone/asymmetric carbonate stretching through the reaction of atmospheric CO_2 with surface KBr hydroxy sites [17]. The bands at 3296 cm^{-1} and 3744 cm^{-1} are expected to arise due to broad O-H and M-OH stretching on the KBr pellet surface respectively.

UV-Visible spectroscopy:

The optical response of the synthesized sillenite material under investigation is analyzed through UV-Visible absorbance spectra in the wavelength range 0 to 2500 nm as depicted in the Fig. 4 (a) .The strong absorbance band appearing in the UV-Visible spectra in the UV range at around 317 nm is significantly due to the absorption edge of Bi triggered through the transition of charge carriers from the fully filled O(2p) orbital at valence band to empty Bi (6p) orbital at conduction band [15,18]. Such observations illustrate strong UV response of the material in the defined wavelength range.

Further the energy bandgap (E_g) of the investigating sample is estimated using Tauc equation $(\boldsymbol{\alpha h\vartheta})^{1/n} = \boldsymbol{A}\,(\boldsymbol{h\vartheta - E_g})$ [19]. As sillenite based materials generally undergo direct allowed transition so the value n is considered as ½ . The E_g value is extracted from the Tauc plot (as shown in Fig. 4 (b)) through extrapolating the tangent line from absorbance onset region to $(\alpha h\vartheta)^2 = 0$ axis and is found to be 2.31 eV. The bandgap of the investigating sample is found to reduce compared to pure $Bi_{12}MnO_{20}$ sillenite is significantly due to induction of some intermediate bands through hybridization interaction between Fe^{3+}/Ni^{3+} 3d-orbitals and O^{2-}/Bi^{3+} 2p-orbital, enhanced visible harvest [18]. Such observations illustrate the suitability of the synthesized sillenite material for photocatalytic application as it displays strong UV light absorption plus visible light sensitivity along with narrow bandgap.

Dielectric features:

Dielectric spectroscopy serves as a powerful technique for exploring the complex interplay among various polarization mechanisms—such as electronic, ionic, dipolar, and space charge polarizations—that collectively govern the dielectric behavior of materials. To examine these effects, the variation of the dielectric constant (ε_r) with frequency at different temperatures was analyzed for the synthesized sillenite $Bi_{12}Mn_{0.5}Fe_{0.25}Ni_{0.25}O_{20-\delta}$ compound, as depicted in Fig. 5. A prominent decrease in ε_r with increasing frequency was observed, a feature typical of dielectric dispersion. This decline can be attributed to the gradual inability of dipoles and charge carriers to follow the rapidly alternating electric field at higher frequencies, whereas at lower frequencies, their alignment with the applied field yields relatively high ε_r values. In the investigated sample, the $6s^2$ lone pair electrons of Bi based oxides are not generally symmetric, they can disturb/weakens the centro-symmetry alignment of the crystal through the creation of local dipoles which later can enhanced the dielectric response of the compound by align themselves along the direction of applied electric perturbations.

The dielectric behavior in the investigated sample also aligns with the Maxwell–Wagner interfacial polarization model, which attributes the high ε_r values at low frequencies to charge accumulation at grain boundaries. As frequency increases, these trapped charges are unable to respond effectively, leading to reduced carrier density and a fall in ε_r. Additionally, the enhanced dielectric response with temperature in the investigating material is also attributing through the hopping of polarons due to the involvement of multivalence ions like Fe, Mn and Ni. Besides the

substitution of aliovalent cations like Fe^{3+} & Ni^{3+} in the tetrahedral site of sillenite with Mn^{4+} ion can leads to the creation of oxygen vacancies which also attribute towards enhancement of dielectric of the sample through triggering the ionic polarizability and forming defect-dipole in the system [20,21].

Impedance spectroscopy:

A very useful analytical technique, namely complex impedance spectroscopy (CIS), is used to investigate the relationship between a material's electrical response and its microstructural characteristics. CIS enables the separation of contributions from grains, grain borders, and electrode interfaces to the overall impedance by applying an external electric field and observing the resulting response across a range of frequencies and temperatures. Thus, this method offers a more profound comprehension of the material's charge transport and relaxation phenomena. The complex impedance activity of the material is analyze using the expression,

$$\mathbf{Z^* = Z' + i\,Z''},$$

Where the real and imaginary components are given by

$Z'' = -\omega R^2 C / (1 + \omega^2\tau^2)$ & $Z' = R / (1 + \omega^2\tau^2)$

Figure 6 (a) illustrate the variation of the real part of impedance (Z′) with temperature and frequency in the depicted range 75^0C to 350^0C. This variation provides important information regarding the electrical behaviour of the sillenite compound under investigation. The sigmoidal variation of Z' indicates the presence of multiple polarisation mechanisms operating within the material. It is nearly constant in the low frequency range up to 1 kHz, then begins to fall with frequency enhancement and nearly reaches saturation at very high frequencies > 1 MHz. A drop in the density of trapped charges at grain boundaries is linked to the observed decline in Z′ with increasing frequency and temperature, suggesting a decrease in resistive barriers to charge transport. Additionally, the lowering of potential barriers and consequent release of space charges are reveal by the convergence of Z′ curves at higher frequencies across various temperatures. This behaviour demonstrates the material's thermally activated conduction mechanism and intricate polarisation dynamics, confirming its Negative Temperature Coefficient of Resistance (NTCR) property.

As shown in Fig. 6 (b), the fluctuation of the imaginary part of impedance (Z") with frequency shows a prominent peak at a specific frequency called the relaxation frequency, after which Z"

steadily falls with increasing frequency. This peak behaviour indicates that the sillenite compound under investigation has relaxing processes. The Z" peak systematically moves towards the higher frequency area as the temperature rises, indicating a thermally induced relaxation process. A distribution of relaxation times is confirmed and the non-Debye nature of the relaxation phenomena is established by the observed broadening and asymmetry of the relaxation peaks as well as the increase in Full Width at Half Maximum (FWHM). Several dynamic mechanisms can be responsible for this behaviour, with oxygen vacancies or defect states playing a major role at higher temperatures and mobile charge carriers predominating at lower temperatures. Z" curves eventually merge in the high-frequency domain, regardless of temperature, suggesting that space charge polarisation has less of an impact at higher frequencies.

To evaluate the respective response of grains, grain boundaries and electrodes in governing the impedance behavior of the investigated sillenite sample, Nyquist plots (Z″ versus Z′ graphs) were analyzed at various temperatures, as illustrated in Fig. 6 (c). The obtained plots display depressed semicircular arcs, indicating a deviation from ideal Debye-type relaxation and confirming the non-Debye nature of the electrical response. To establish a correlation between the electrical characteristics and the microstructural attributes, the Nyquist spectra were modeled using different RC equivalent circuits via the ZSIMWIN simulation software, as shown in the inset of Fig. 7. To account for the deviation from Debye behavior, a constant phase element (Q) was incorporated into the circuit model. The experimental data for the investigated sillenite compound in the temperature range (75^0C - 150^0C) exhibited an excellent fit with an equivalent circuit consisting of (CQR) and (CR) connected in series, suggesting predominance of grains and grain boundaries contribution while in the temperature range (175^0C – 350^0C), the better fitting is obtained with three equivalent circuits (CQR), (CR) and (CR) connected in series, suggesting the involvement of grains, grain boundaries and electroding effect [22,23].

Modulus spectroscopy:

To obtain a thorough grasp of the electrical, relaxation, and transport properties of the material under study, the modulus spectroscopic approach was utilised. By differentiating between components with identical resistance but different capacitance, this method effectively reduces the impact of electrode or grain boundary effects. A better understanding of the

material's bulk electrical behaviour is made possible by this suppression. The frequency-dependent variation of the real part of the electric modulus (M′) at specific temperatures in the sillenite compound under investigation (Fig. 7 (a)) shows that M′ stays almost constant in the low-frequency region (< 10 kHz), confirming the minimal contribution of electrode effects. At higher frequencies (> 10 kHz), however, a noticeable dispersion in M′ spectra suggests that short-range mobile charge carriers actively participate in the conduction process. This behaviour is explained by the enhanced mobility of charges under the influence of an external perturbation due to the lack of a restoring force.

As shown in Fig. 7 (b), the frequency-dependent fluctuation of the imaginary component of the electric modulus (M") at various temperatures provides important information about the material's relaxation dynamics. The existence of relaxation processes is confirmed by the observation that M" rises with frequency and reaches a peak (M"max) at a particular frequency. With increasing temperature, this peak shifts toward the higher frequency region, signifying a transition of mobile charge carriers from long-range to short-range motion and suggesting a thermally activated hopping conduction mechanism. The temperature-dependent variation in the height and position of the relaxation peak further implies a change in the material's capacitance. Moreover, the asymmetric broadening of M" spectra with rising temperature supports the presence of non-Debye type relaxation behavior, indicating a distribution of relaxation times within the system [24,25].

AC conductivity:

The conductivity spectra of the investigated sillenite compound, namely $Bi_{12}Mn_{0.5}Fe_{0.25}Ni_{0.25}O_{20-\delta}$, is found to consist of two regions (i) Flatter region (DC conductivity) and (ii) sharply raising frequency dependent region (AC conductivity) as depicted in Fig. 8. The observed variation of conductivity spectra is consistent with universal Jonscher's law followed by the equation $\sigma(\omega) = \sigma_{dc} + A\omega^n$ [26]. In the investigated sample, the observed enhancement of conductivity at elevated frequency is due to the substitution of mixed valence ions namely (Fe^{3+}/Fe^{2+}) and (Ni^{3+}/Ni^{2+}) which can introduce some shallow energy level to boost the hopping conduction of charge carriers through reducing impedance [27,28]. Besides the enhancement of conductivity with temperature, it is noticed that the slope of the conductivity spectra increases with enhancement of temperature. Such observation suggest enhancement of hopping frequency with temperature. As temperature rises, the thermally activated charge transporter easily

overcomes the barrier field, resulting in enhancement of hopping frequency along with conductivity. In the investigated sillenite compound, the substitution of Fe^{3+} and Ni^{3+} can distort the oxygen sublattice, promoting the polaronic conduction mechanism in the system through enhancing the hopping probability of polarons between the localized sites [27,28].

Leakage current and temperature sensor:

The leakage feature and type of carriers participate in the conduction mechanism is investigated through analysis the variation of leakage current (I) with applied voltage (V) as depicted in Fig. 9. It is noticed that the leakage current is increasing in non-linear manner with applied voltage. Such observation is pointing towards the investigated material's semiconducting character. Besides it's also found that the non-linearity of the sample is enhanced further with temperature. The involvement of multivalence ions like Fe and Ni in the investigated sample boosting the carrier transportation via electron hopping between $Fe^{3+} \leftrightarrow Fe^{2+}$ and $Ni^{3+} \leftrightarrow Ni^{2+}$, which elevates the leakage current in the present investigated sample. The involvement of multivalence ions can also make the system n-type. Besides the NTCR type conduction feature is once again clarify through I-V investigation. The NTCR feature of the investigated material also opens up the possibility for temperature sensor oriented application like thermistor. To check the possible application towards thermistor, the variation of resistance (R) with temperature (T) is investigated as depicted in Fig. 10 through incorporating Steinhart Equation $\mathbf{\ln R = \ln R_0 + \beta (1/T - 1/T_0)}$ [13,29], where β is thermistor coefficient and other symbol possess their usual meaning. In addition, the temperature sensitivity factor (α) of the investigated material is extracted from the Fig. 12 using the relation $R_T = \alpha \exp(1/T)$ [29]. The value of β and α for the investigated sample are found to be 4157.3 Kelvin and – 0.241 respectively.

Magnetic feature:

The magnetic ordering/disordering in the investigated sillenite compound is inspected through study the variation of magnetic moment per unit mass with applied magnetic field in the range – 15000 Oe to + 15000 Oe as depicted in the Fig. 11. The investigation reveals the inspected sillenite compound exhibit weak ferromagnetism with retentivity $M_R = 0.0050$ emu/gm and coercivity $H_C = 115.84$ Oe. Pure Sillenite materials are generally classified as weak paramagnetic in nature, the emergence of weak ferromagnetism in the synthesized sillenite compound must associated directly/indirectly with the substitution of transition metal ions Fe^{3+}

and Ni^{3+} in the host environment. The substitution of Fe^{3+} and Ni^{3+} at the Mn^{4+} site can induce spin canting according to Dzyaloshinskii–Moriya (DM) interaction mechanism [30,31], leading to weak ferromagnetic channel within local environment. As sillenites are prone to forming oxygen vacancies during cation substitution at Mn site, it is expected to cause valency fluctuation in Fe and Ni which later can trigger double exchange interaction path via Fe^{2+}-O-Fe^{3+} and Ni^{2+}-O-Ni^{3+} causing weak ferromagnetism in sillenite.

In the investigation of M-H curve for the inspected sample, it is observed that saturation in magnetization is not arising even at ± 15000 Oe applied field. To extract the saturation magnetization and other associated parameters, we have incorporate Law of approach to saturation (LAS) method [32,33] through fitting the experimental data (as shown in Fig. 12) with some of the standard LAS models such as

Akulov's Model: $M = M_s [1-b/H^2]$.....(I)

Neel's Model: $M = M_s [1- a/H- b/H^2]$……..(II)

Brown's Model: $M = M_s [1- a/H- b/H^2] + \chi H$…….(III)

Grosinger's Model: $M = M_s [1- a/H- b/H^2- c/H^3] + \chi H$……..(IV)

Here, a, b & c represents empirical fitting coefficient associate with non-linear response of magnetic moments as an inverse power of applied magnetic field H. The symbol χ represent magnetic susceptibility, which assign the linear response of magnetic moments with applied magnetic field H in the high field regime.

Through the fitting of experimental data, it is noticed that Akulov's model is derivates from the concept of saturation. Although the deviation is found less for Neel's model and Brown model, but the better fitting is obtained for Grosinger's model with $(chi)^2$ value 1.474×10^{-7}. The detailed values of the parameters obtained through fitting of aforesaid model are tabulated as depicted in Table 3.

Conclusion:

The present investigation established a successful synthesization of a new aliovalent substituted $Bi_{12}MnO_{20}$ sillenite-based oxides through an optimized solid-state reaction at 800°C. Comprehensive structural analysis via Rietveld refinement unequivocally confirms the formation

of the compound with cubic symmetry (space group *I*23, a = b = c = 10.105 Å) with excellent reliability (R_p = 9.05%, R_{wp} = 15.95%, R_{exp} = 12.11% and χ^2 = 1.74), complemented by crystallite size 1.344 nm and lattice strain 0.0162 extracted through Williamson-Hall plot. The morphological analysis through SEM/EDX and FTIR analysis unequivocally validate phase purity, polycrystallinity, elemental stoichiometry (Bi, Mn, Fe, Ni, O), and characteristic phonon-lattice modes of vibration (400–600 cm^{-1}). UV-Visible spectroscopic analysis highlights reduced direct bandgap (2.31 eV) of the synthesized sillenite compound, signifies enhance photodetection/photocatalytic abilities relative to undoped $Bi_{12}MnO_{20}$. The Dielectric/Electrical characterization reveals a strong dielectric response aligned with the Maxwell-Wagner model, featuring temperature-dependent polaron hopping, sigmoidal multi-polarization (Z'), non-Debye relaxation (Z''), and NTCR feature, with conduction mechanism align with Jonscher's power law and dominated by short-range carriers at high frequencies. While I-V characteristic spectra confirms n-type semiconductivity boosted by multivalent ions, with NTCR thermistor feature (β = 4157.3 K) extracted through Steinhart-Hart equation. Weak ferromagnetism with M_R = 0.005 emu/g, H_c = 115.84 Oe and M_s = 0.839 emu/g emerges through double exchange interaction trigger via Fe/Ni substituent. The interconnected structural, electrical, optical and magnetic feature of the synthesized sillenite sample make it a preferable candidate for multifunctional applications especially in photodetectors, precision thermistors.

References:

[1] Y. Hu, D.C. Sinclair, Relaxor-like Dielectric Behavior in Stoichiometric Sillenite Bi 12 SiO 20, 12 (2013).

[2] B.M.O.M. Si, Processing and Dielectric Properties of Sillenite Compounds, 904 (2001) 2900–2904.

[3] O. Baaloudj, N.-N. Vu, A.A. Assadi, V.Q. Le, P. Nguyen-Tri, Recent advances in designing and developing efficient sillenite-based materials for photocatalytic applications, Adv. Colloid Interface Sci. 327 (2024) 103136. https://doi.org/https://doi.org/10.1016/j.cis.2024.103136.

[4] S. Chehab, P. Conflant, M. Drache, J. Boivin, G. Mcdonald, Solid-state reaction pathways of Sillenite-phase formation studied by high-temperature X-ray diffractometry and differential thermal analysis, 38 (2003) 875–897. https://doi.org/10.1016/S0025-5408(03)00025-4.

[5] M. Isik, G. Surucu, A. Gencer, N.M. Gasanly, Electronic , optical and thermodynamic characteristics of Bi 12 SiO 20 sillenite : First principle calculations, Mater. Chem. Phys. 267 (2021) 124711. https://doi.org/10.1016/j.matchemphys.2021.124711.

[6] P.M. Woodward, J. Goldberger, M.W. Stoltzfus, H.W. Eng, R.A. Ricciardo, P.N. Santhosh, P. Karen, A.R. Moodenbaugh, Electronic, magnetic, and structural properties of Sr2MnRuO6 and LaSrMnRuO6 double perovskites, J. Am. Ceram. Soc. 91 (2008) 1796–1806.

[7] Y. Belik, T. Kharlamova, A. Vodyankin, V. Svetlichnyi, O. Vodyankina, Mechanical activation for soft synthesis of bismuth silicates, Ceram. Int. 46 (2020) 10797–10806.

[8] A.A. Ballman, H. Brown, P.K. Tien, R.J. Martin, The growth of single crystalline waveguiding thin films of piezoelectric sillenites, J. Cryst. Growth 20 (1973) 251–255. https://doi.org/https://doi.org/10.1016/0022-0248(73)90013-4.

[9] J.E. Alfonso, M.J. Martín, V. Volkov, C. Zaldo, M. Aguilo, M.F. Da Silva, J.C. Soares, Photoconductive Bi12MO20-type films prepared by pulsed laser deposition, J. Mater. Res. 14 (1999) 4409–4417.

[10] L. Wiehl, A. Friedrich, E. Haussühl, W. Morgenroth, A. Grzechnik, K. Friese, B. Winkler, K. Refson, V. Milman, Structural compression and vibrational properties ofBi12SiO20 sillenite from experiment and theory, J. Phys. Condens. Matter 22 (2010) 505401.

[11] Y. Hu, D.C. Sinclair, Relaxor-like Dielectric Behavior in Stoichiometric Sillenite Bi12SiO20, Chem. Mater. 25 (2013) 48–54. https://doi.org/10.1021/cm3031363.

[12] M. Valant, D. Suvorov, A Stoichiometric Model for Sillenites, Chem. Mater. 14 (2002) 3471–3476. https://doi.org/10.1021/cm021173l.

[13] H. Chouhan, S. Prasad, S. Parthasarathy, R. Chakravarty, B.N. Parida, Unveiling the potential of a novel inorganic perovskite for NTC thermistor and energy-storage applications, Inorg. Chem. Commun. 170 (2024) 113127. https://doi.org/10.1016/j.inoche.2024.113127.

[14] R. Shukla, P. Saha, A.B. Shinde, P.S.R. Krishna, P.D. Babu, A.K. Tyagi, S.N. Achary, D. Santamaría-Perez, T. Marqueño, J. Ruiz-Fuertes, C. Popescu, D. Errandonea, On formation and evolution of structure of sillenite type Bi25FeO40 phase with temperature and pressure, J. Alloys Compd. 1020 (2025) 179528. https://doi.org/https://doi.org/10.1016/j.jallcom.2025.179528.

[15] X. Wu, M. Li, J. Li, G. Zhang, S. Yin, A sillenite-type Bi12MnO20 photocatalyst: UV, visible and infrared lights responsive photocatalytic properties induced by the hybridization of Mn 3d and O 2p orbitals, Appl. Catal. B Environ. 219 (2017) 132–141. https://doi.org/https://doi.org/10.1016/j.apcatb.2017.07.025.

[16] B.S. Tripathy, R.N.P. Choudhary, B. Umapathi, P. Nayak, S.K. Parida, Structure, dielectric, vibrational, and optical properties of lead-free double perovskite Bi2FeMnO6, Ferroelectrics 618 (2024) 47–62. https://doi.org/10.1080/00150193.2023.2271314.

[17] A.H. Lahuri, M.A. Yarmo, Study of CO2Adsorption Time for Carbonate Species and Linear CO2Formations onto Bimetallic CaO/Fe2O3by Infrared Spectroscopy, Sains Malaysiana 51 (2022) 507–517. https://doi.org/10.17576/jsm-2022-5102-15.

[18] F. Sharmin, M.A. Basith, Simple Low Temperature Technique to Synthesize Sillenite Bismuth Ferrite with Promising Photocatalytic Performance., ACS Omega 7 (2022) 34901–34911. https://doi.org/10.1021/acsomega.2c03457.

[19] P. Makuła, M. Pacia, W. Macyk, How To Correctly Determine the Band Gap Energy of Modified Semiconductor Photocatalysts Based on UV–Vis Spectra, J. Phys. Chem. Lett. 9 (2018) 6814–6817. https://doi.org/10.1021/acs.jpclett.8b02892.

[20] S. Bhattacharjee, B. Mohanty, N.C. Nayak, R.K. Parida, B.N. Parida, Optical, dielectric and magnetic investigation of vanadium based double perovskite, Mater. Sci. Semicond.

Process. 123 (2021) 105503.

[21] S. Bhattacharjee, S. Sen, R.K. Parida, S.K. Deb, R. Deb, R. Dutta, B.N. Parida, Synthesis and characterization of Ba-doped vanadium-based double perovskite for multifunctional applications, Mater. Today Proc. (2022).

[22] S. Bhattacharjee, R.K. Parida, B.N. Parida, Investigation of multifunction features of double perovskite oxide A2FeVO6 (where A = Ba, Ca), Phys. B Condens. Matter 659 (2023) 414849. https://doi.org/10.1016/j.physb.2023.414849.

[23] S. Bhattacharjee, B. Mohanty, R.K. Parida, B.N. Parida, Dielectric and transport properties of "Sr" modified lead free double perovskite, Mater. Today Proc. 35 (2021) 94–96. https://doi.org/10.1016/j.matpr.2020.03.070.

[24] F. Brahma, B. Mohanty, S. Bhattacharjee, R.L. Hota, R.K. Parida, N. Parida, Materials Science in Semiconductor Processing Investigation of multifunctional characteristics in SmFeO 3 -BaTiO 3 perovskite system for devices, 135 (2021). https://doi.org/10.1016/j.mssp.2021.106071.

[25] B. Mohanty, S. Bhattacharjee, N.C. Nayak, R.K. Parida, B.N. Parida, Dielectric, magnetic and optical study of La-doped BFO-BST ceramic for multifunctional applications, Mater. Sci. Semicond. Process. 128 (2021) 105720. https://doi.org/10.1016/j.mssp.2021.105720.

[26] S.K. Satpathy, N.K. Mohanty, A.K. Behera, K.C. Patra, B. Behera, P. Nayak, J. Vihar, Effect of Electrical Properties on Gd modified BiFeO 3 -PbZrO 3, (n.d.).

[27] F. Tayari, I. Nassar, Investigating Fe-doped Ba0.67Ni0.33Mn1−xFexO3 (x = 0, 0.2) ceramics: insights into electrical and dielectric behaviors, (2024) 12561–12573. https://doi.org/10.1039/d4ra01581a.

[28] D.S. Vavilapalli, A.A. Melvin, F. Bellarmine, R. Mannam, S. Velaga, H.K. Poswal, A. Dixit, M.S. Ramachandra Rao, S. Singh, Growth of sillenite Bi(12)FeO(20) single crystals: structural, thermal, optical, photocatalytic features and first principle calculations., Sci. Rep. 10 (2020) 22052. https://doi.org/10.1038/s41598-020-78598-3.

[29] S.B. Harshavardhan, C. Saurabh, P.R.K. Parida, An investigation of new inorganic perovskite oriented material for NTC - thermistor and other multifunctional application, Appl. Phys. A 131 (2025) 1–14. https://doi.org/10.1007/s00339-025-08263-x.

[30] N.D. Long, C. V Ha, Q.N. Pham, E. Riviere, N. Tran, N.T.M. Hong, D. V Karpinsky, L.T. Ha, P.T. Thanh, T. Six, P.M. An, P.T. Tho, N.Q. Hai, Weak ferromagnetism in

morphotropic phase boundary of BiFeO3-based materials, J. Alloys Compd. 986 (2024) 174169. https://doi.org/https://doi.org/10.1016/j.jallcom.2024.174169.

[31] C.A. Crawford, T.W. Surta, L.M. Daniels, S. Savvin, H. Niu, J. Alaria, J.B. Claridge, M.J. Rosseinsky, Evolution of Magnetic Symmetry through the BiFeO(3)-Ca(2)Fe(4/3)W(2/3)O(6) Phase Diagram., Inorg. Chem. 64 (2025) 15413–15423. https://doi.org/10.1021/acs.inorgchem.5c01516.

[32] S. Sahoo, S. Mishra, H. Chouhan, Structural, dielectric, optical, and magnetic properties of ferrite-double perovskites for potential industrial applications, (2025) 27467–27485. https://doi.org/10.1039/d5ra02892b.

[33] H. Chouhan, S. Prasad, R.K. Parida, B.N. Parida, A comprehensive study on structural , transport and magnetic properties of novel inorganic perovskite for multifunctional applications, Ceram. Int. (2025). https://doi.org/10.1016/j.ceramint.2025.04.018.

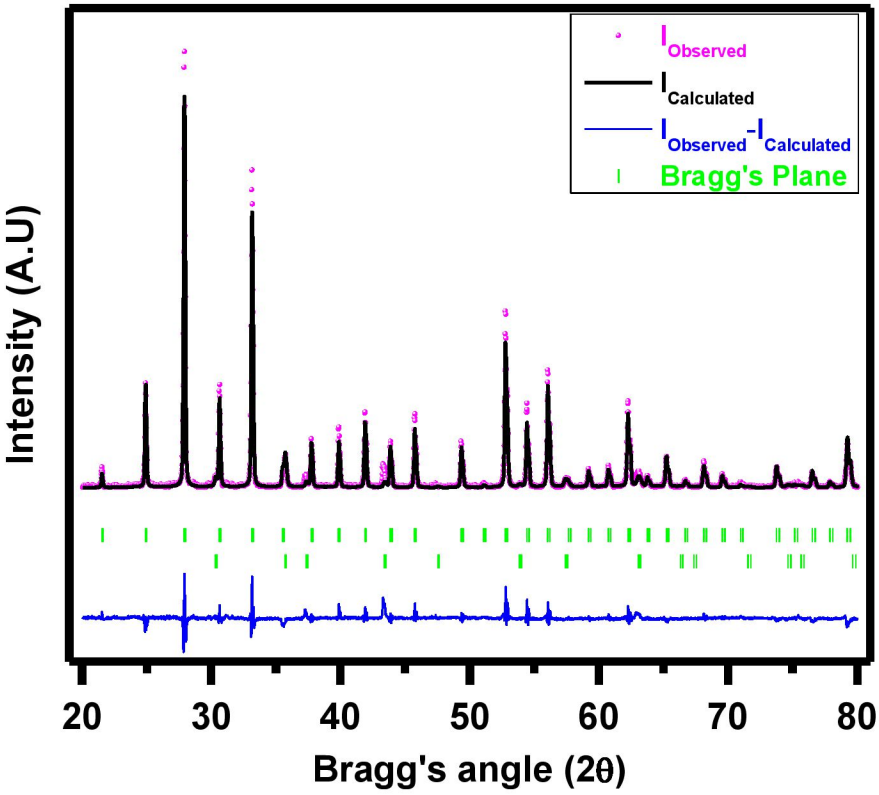


Fig. 1 (a): Reitveld refined XRD profile of the investigated Sillenite sample

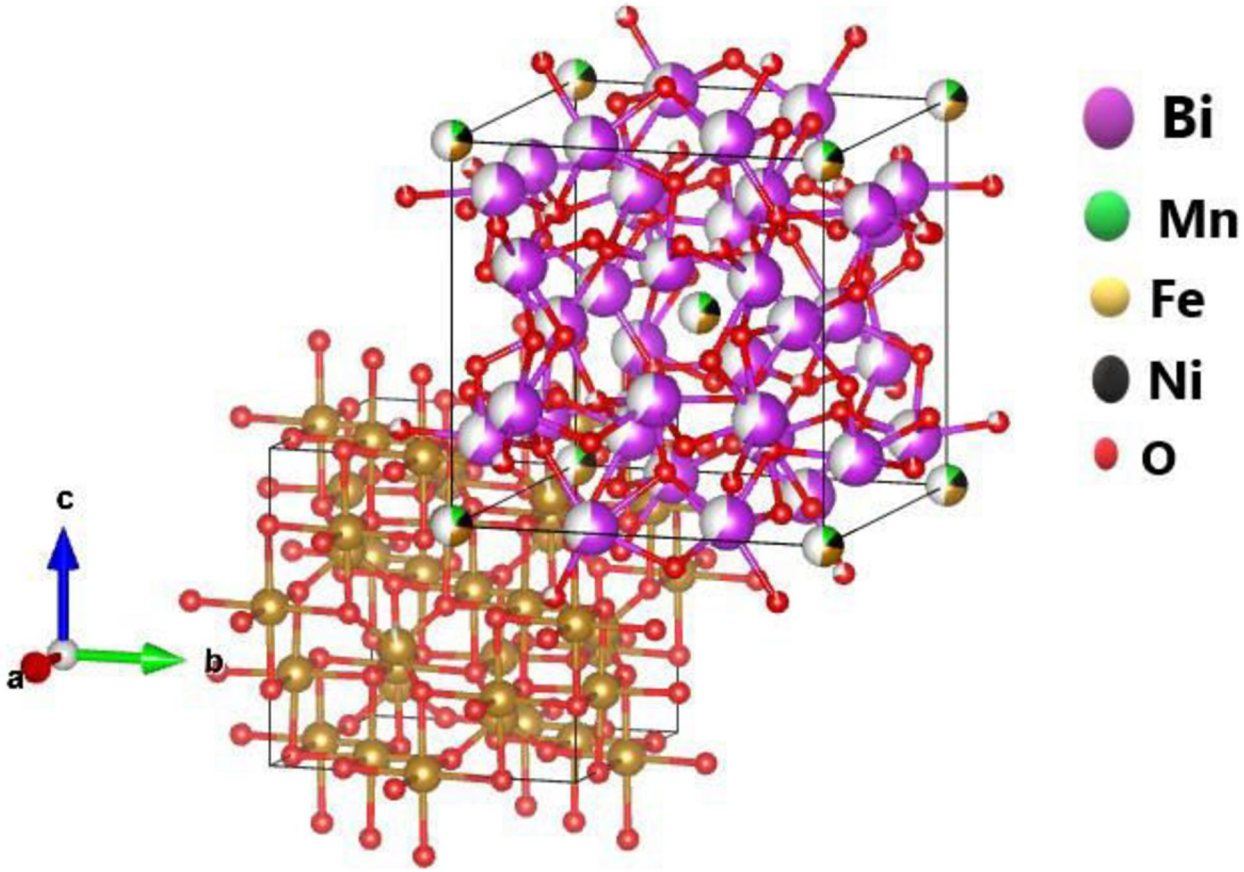


Fig. 1 (b): Schematic structural configuration of the investigated Sillenite sample

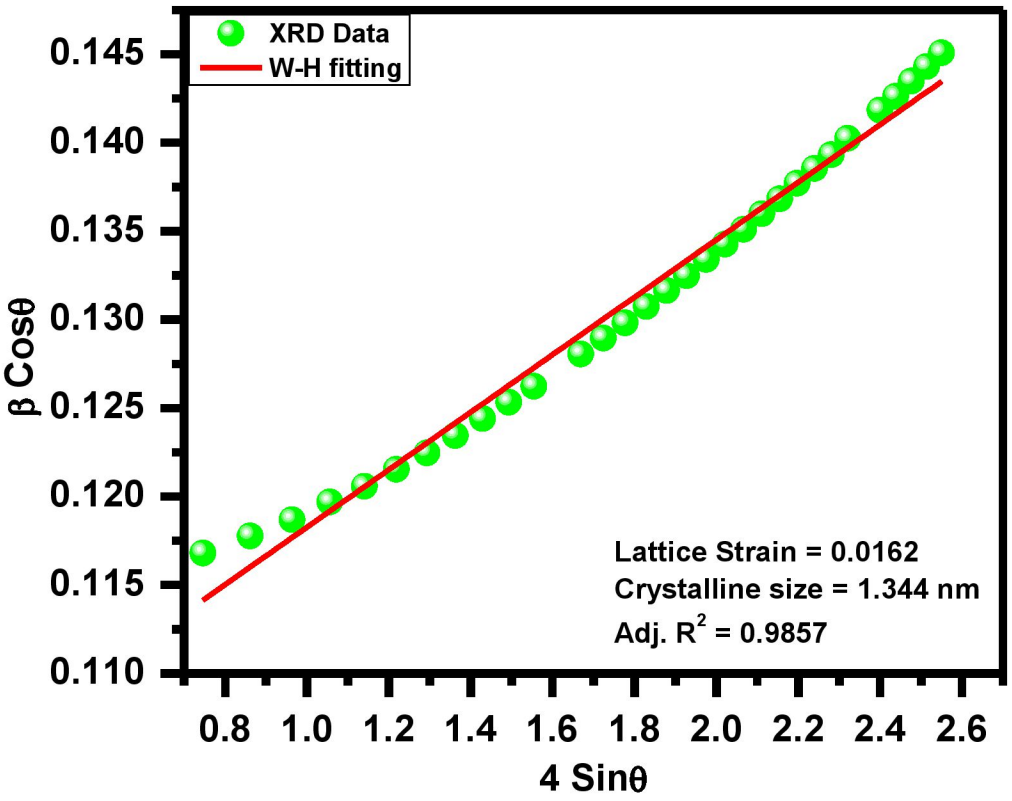


Fig. 1 (c): Willamson-Hall plot of the investigated XRD data

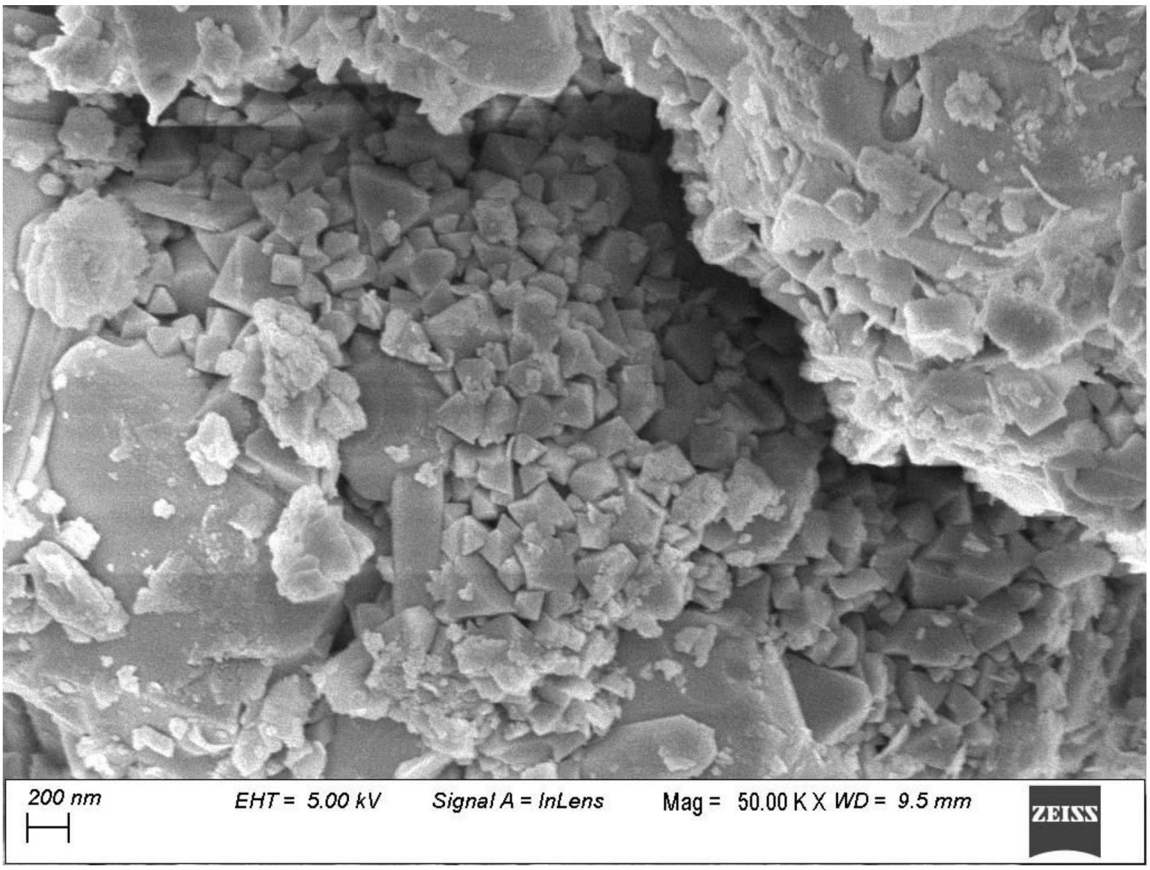


Fig. 2 (a): SEM morphology of the inspected Sillenite sample

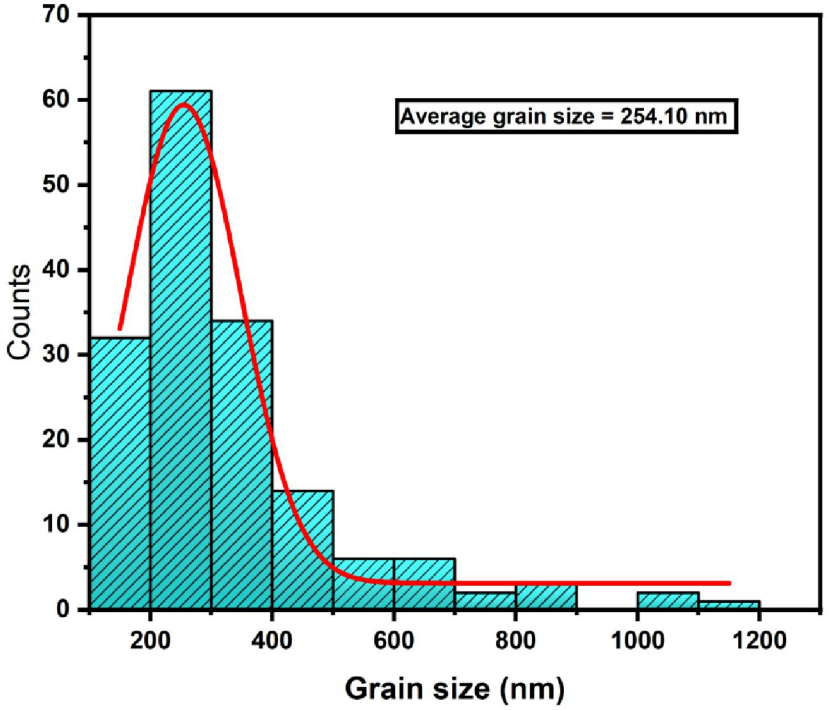


Fig. 2 (b): Histogram mapping for the grain size of the investigated Sillenite sample

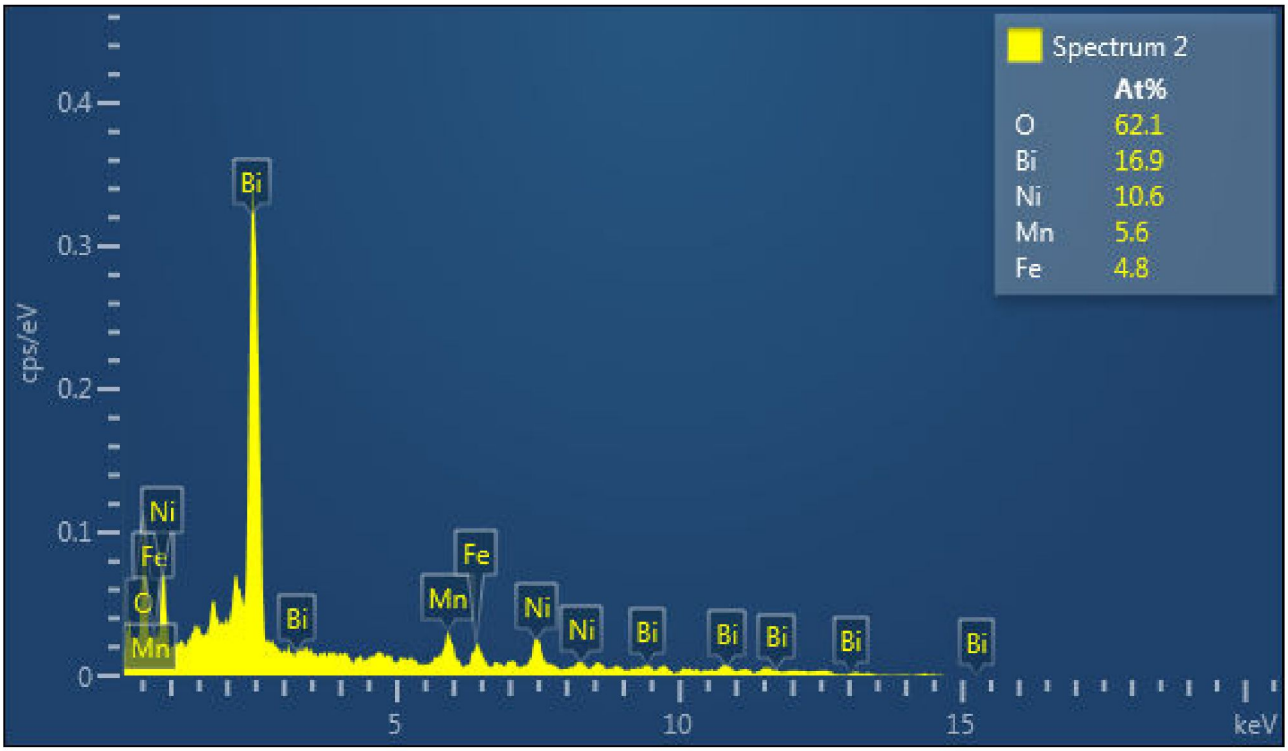


Fig. 2 (c): EDX spectra of the investigated Sillenite sample

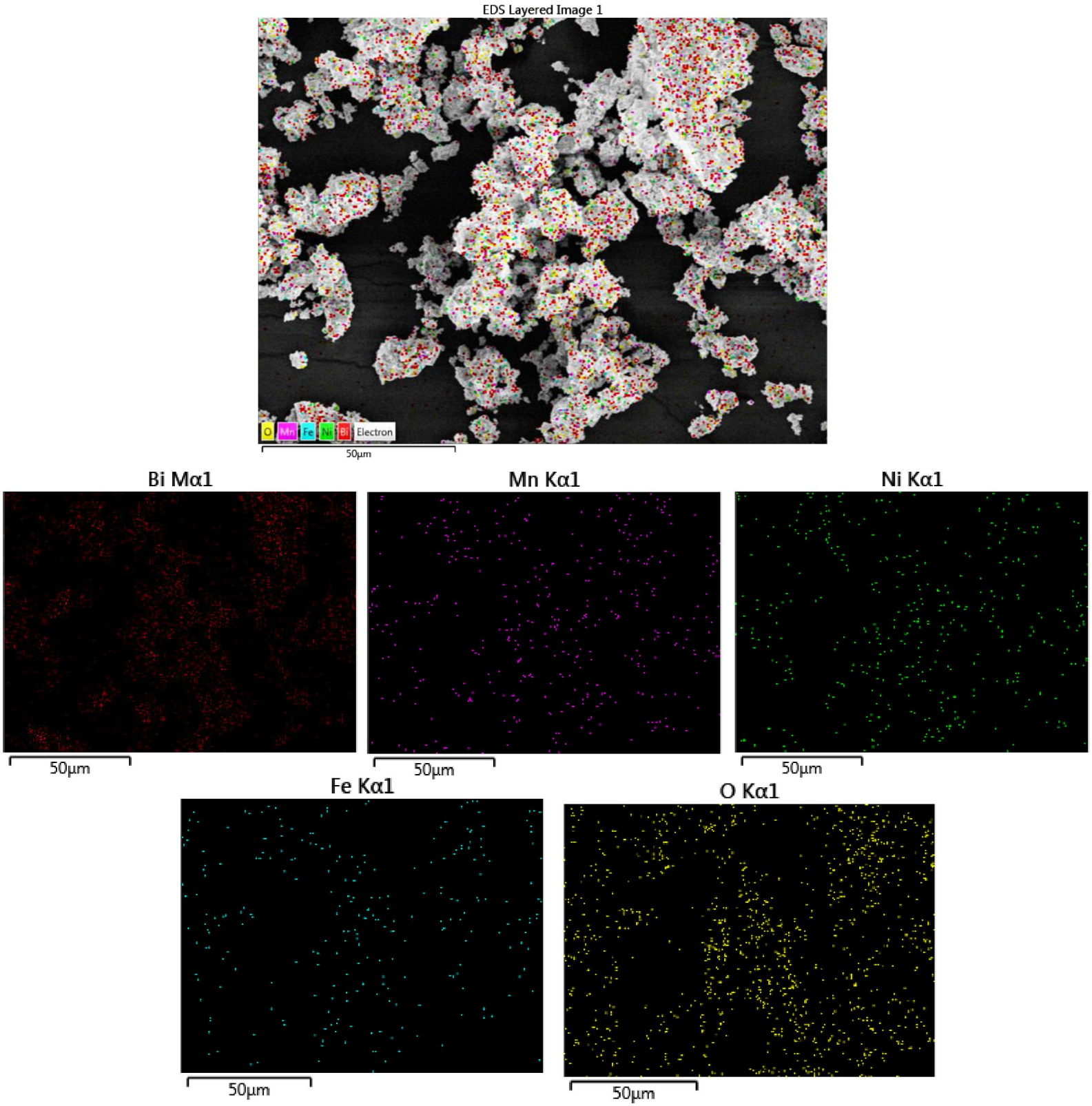


Fig. 2 (d): Color mapping of involved elements in the inspected Sillenite sample

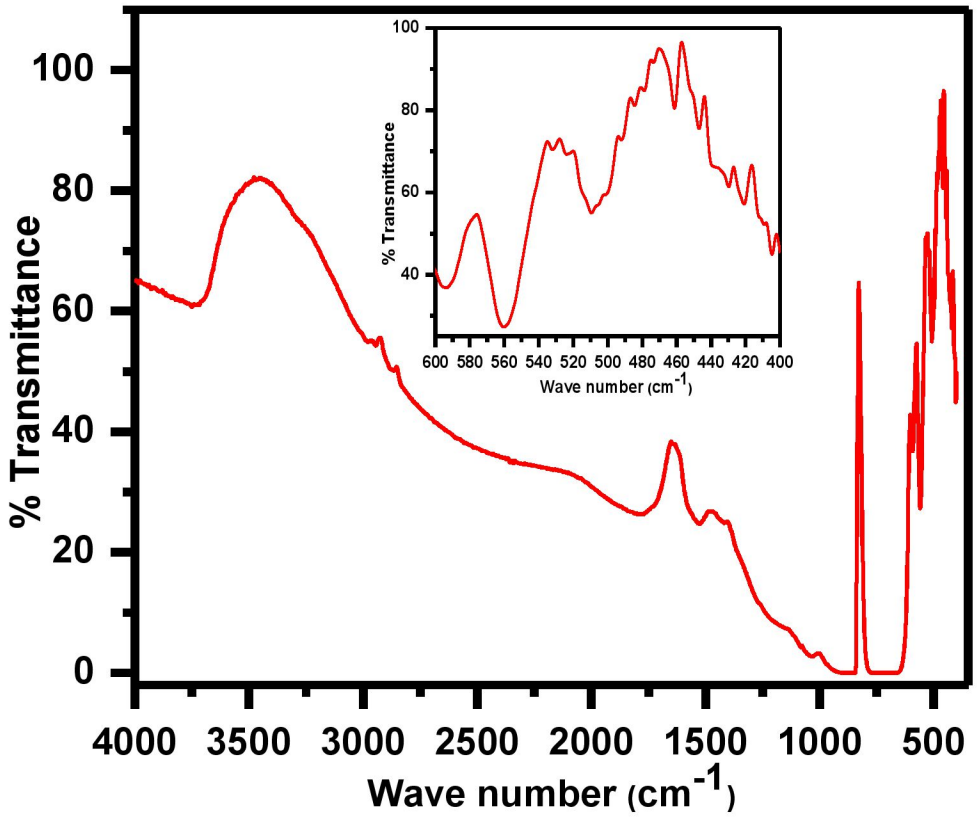


Fig. 3: FTIR spectra of the inspected Sillenite sample

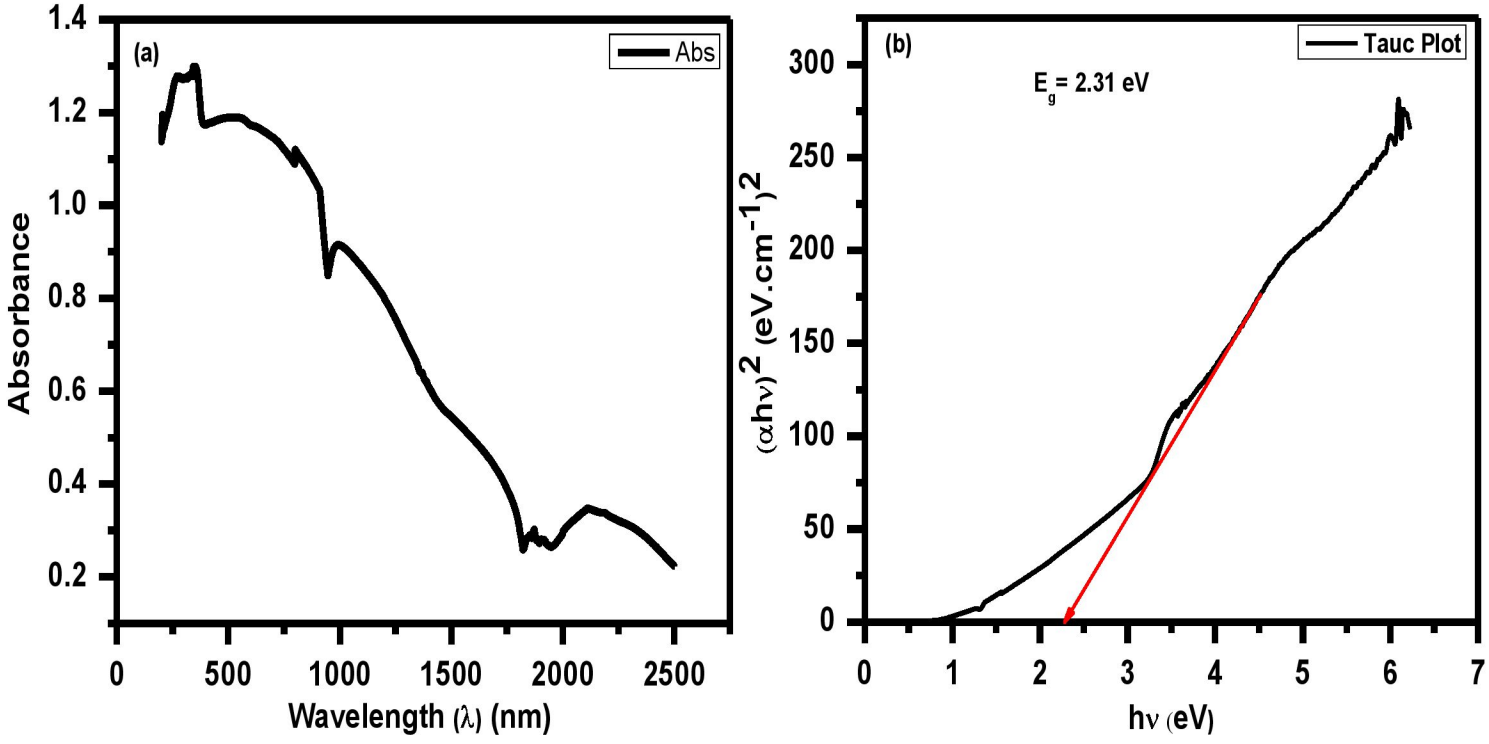


Fig. 4: (a) UV-Visible Absorbance spectra (b) Tauc Plot of the inspected Sillenite sample

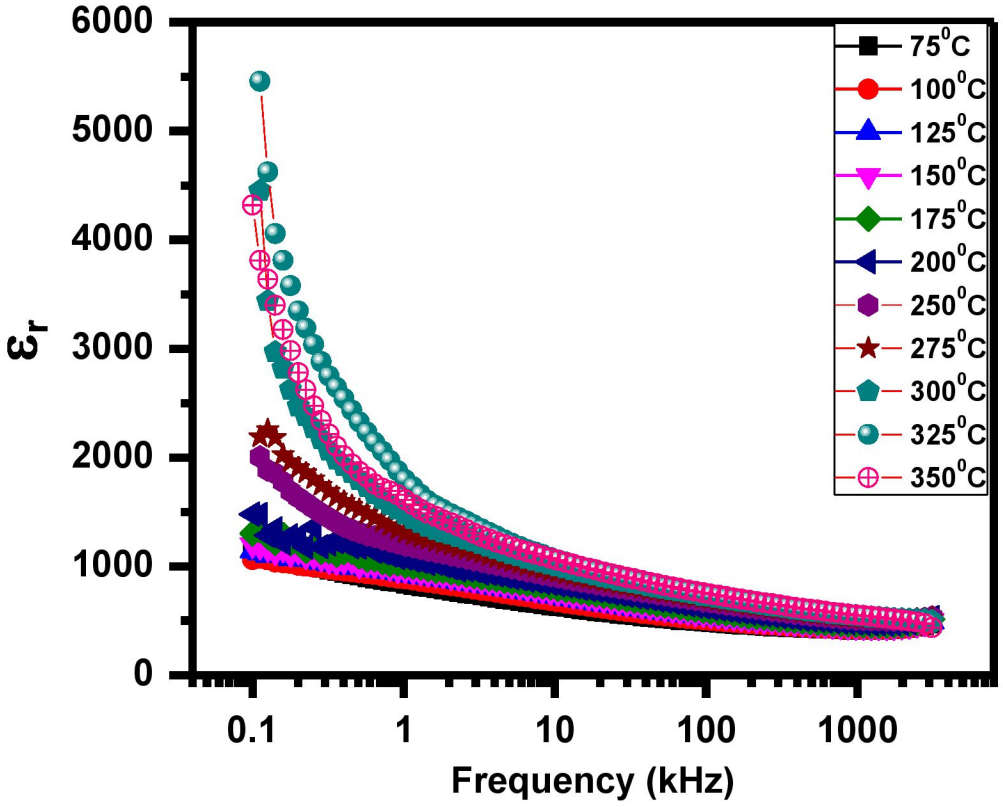


Fig. 5: Dielectric spectra of the investigated sillenite sample

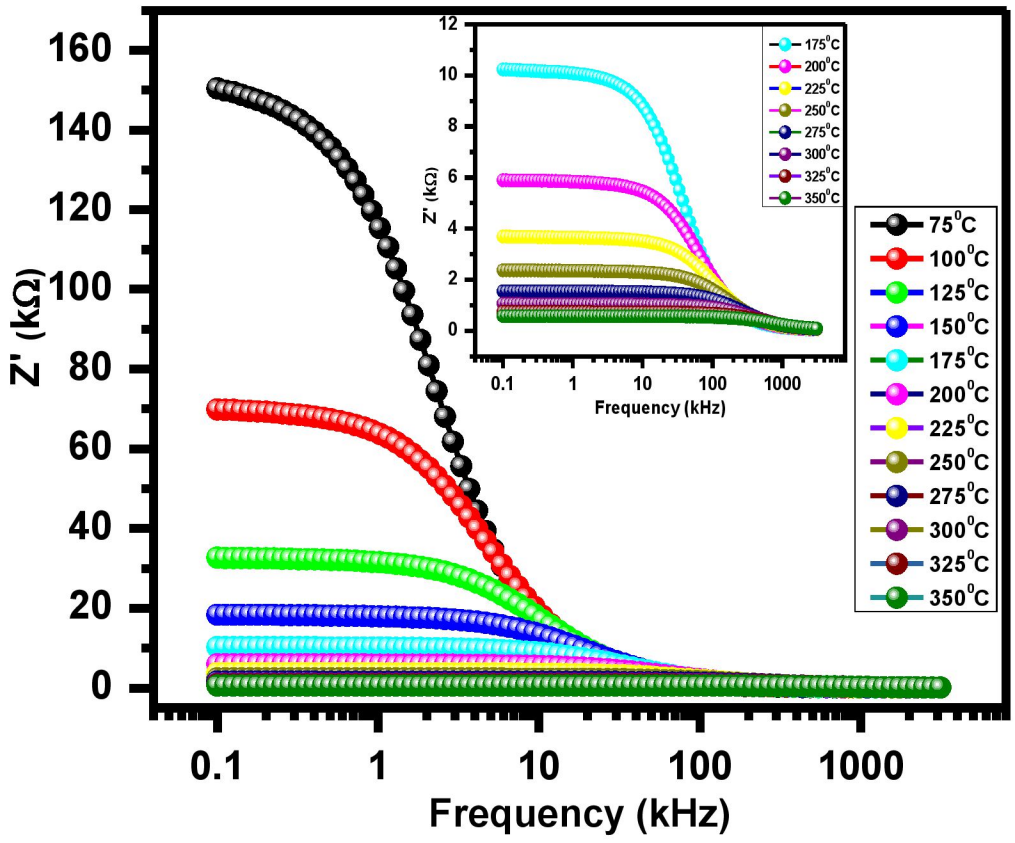


Fig.6 (a): Variation of Z' with frequency in the specific temperature range for investigated sillenite sample

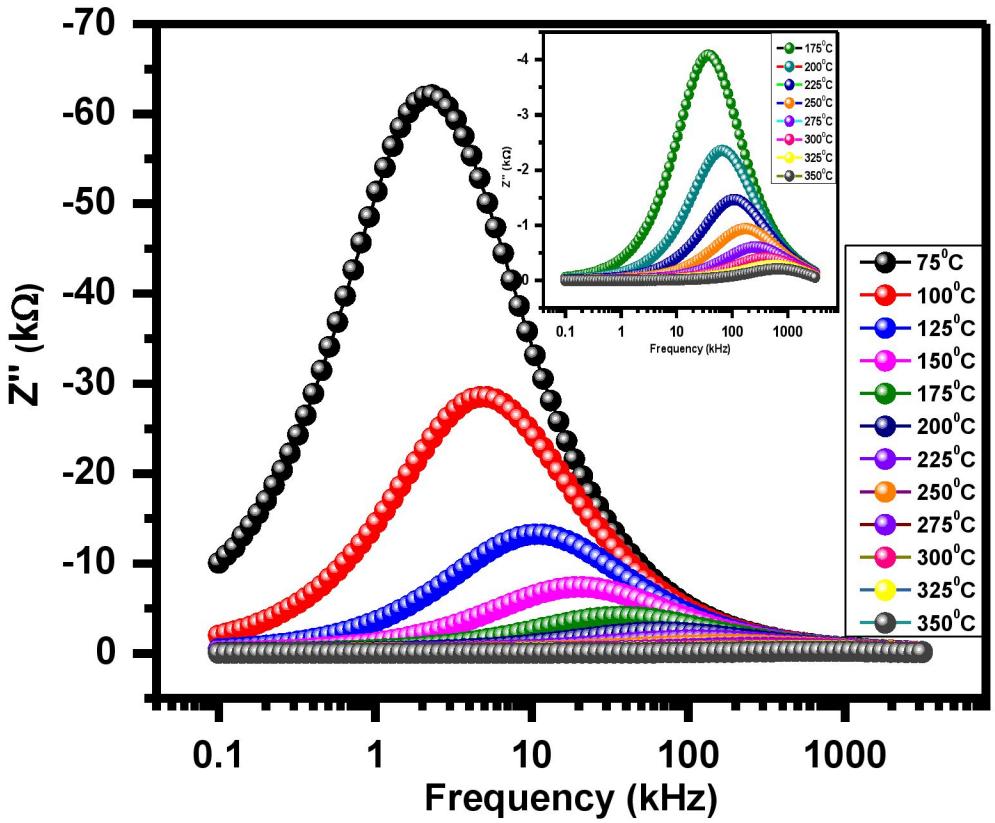


Fig. 6 (b): Variation of Z'' with frequency in the specific temperature range for investigated sillenite sample

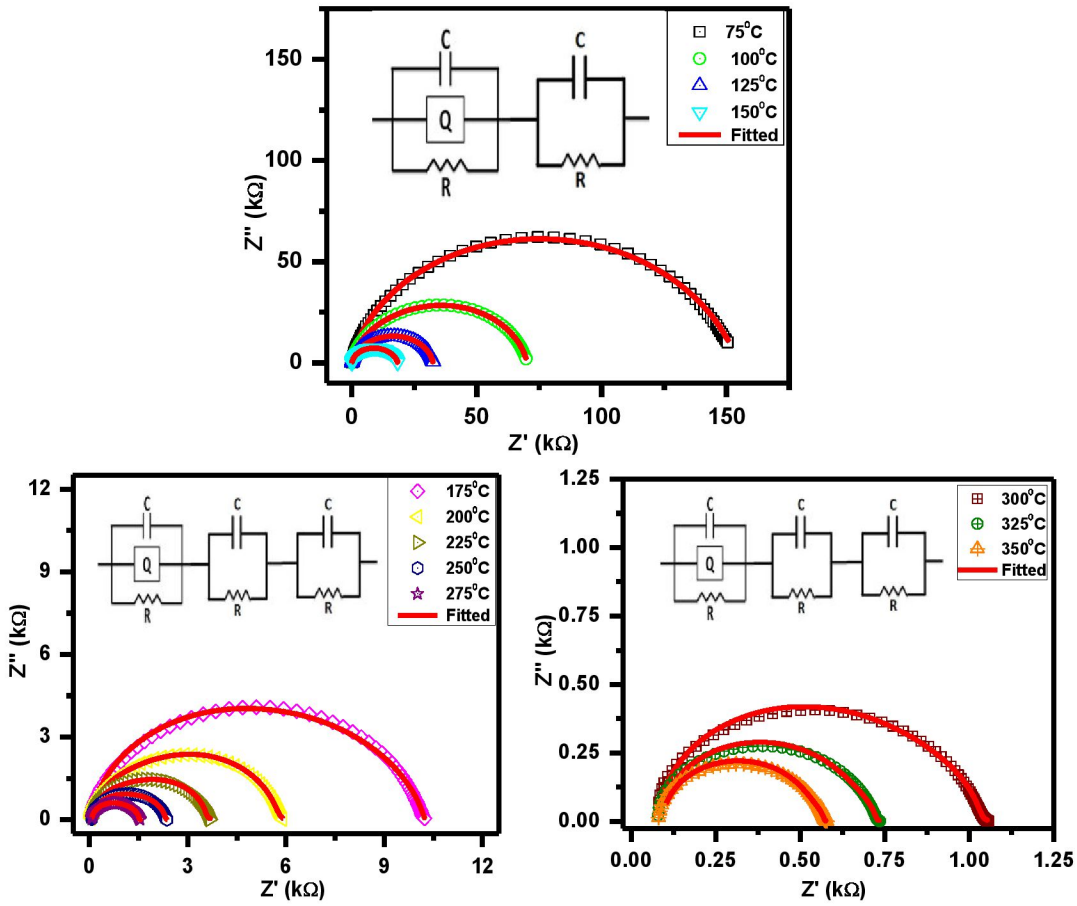


Fig. 6 (c): Nyquist spectra of investigated sillenite sample

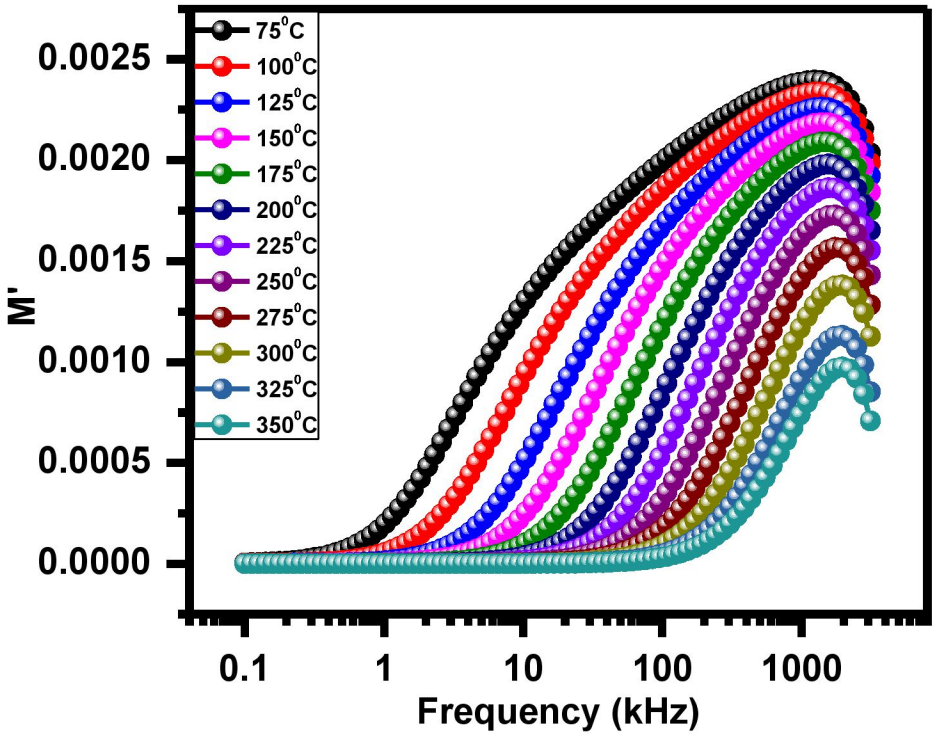


Fig. 7 (a): Variation of M' with frequency in the specific temperature range for investigated sillenite sample

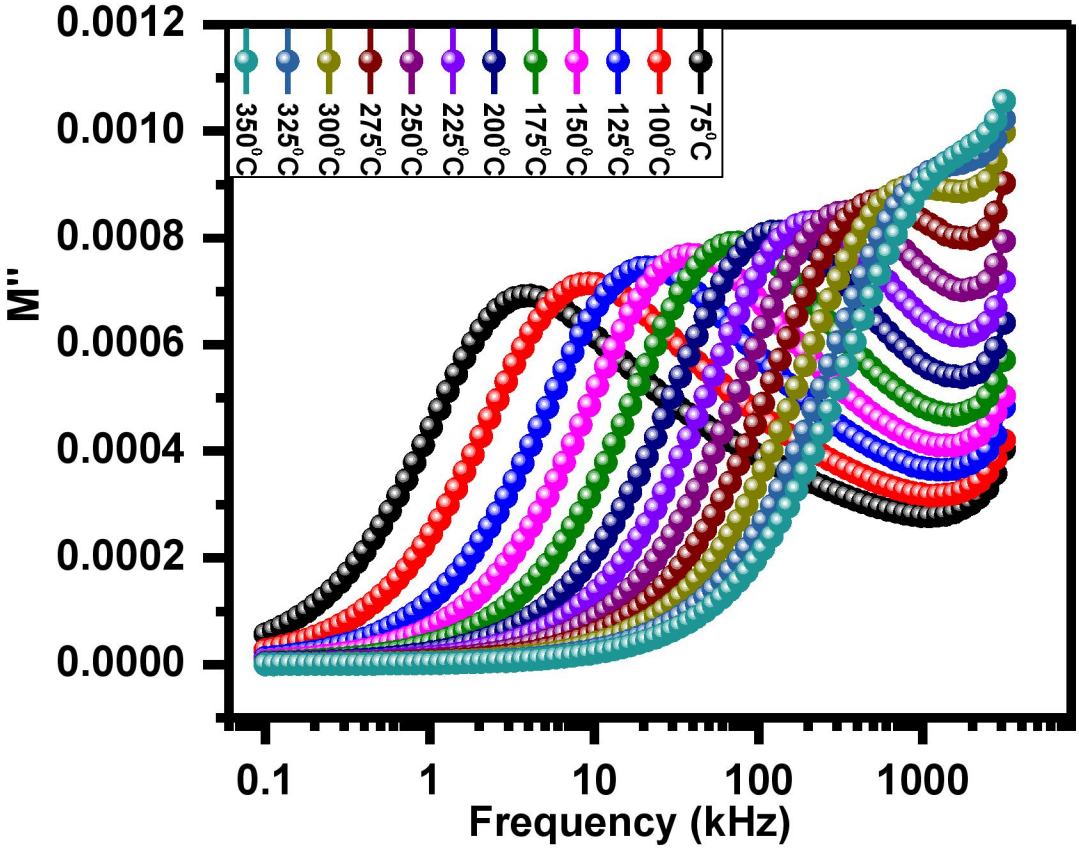


Fig. 7 (b): Variation of M'' with frequency in the specific temperature range for investigated sillenite sample

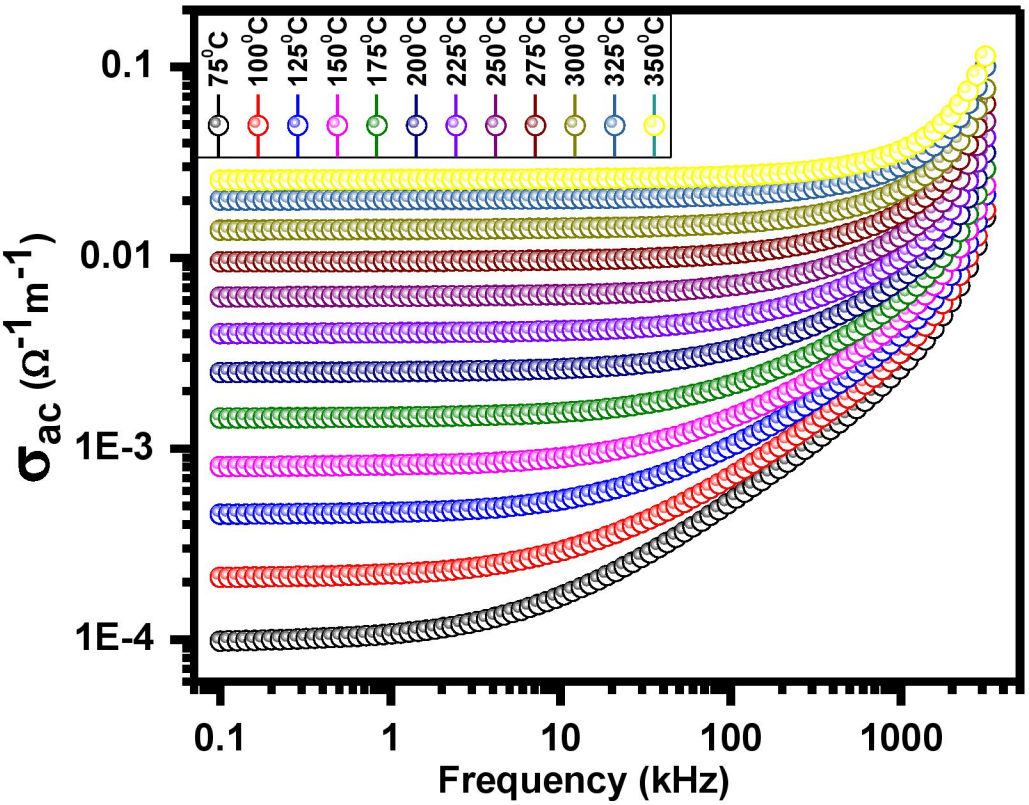


Fig. 8: Variation of AC conductivity of the investigated sillenite sample with frequency in the specified temperature range

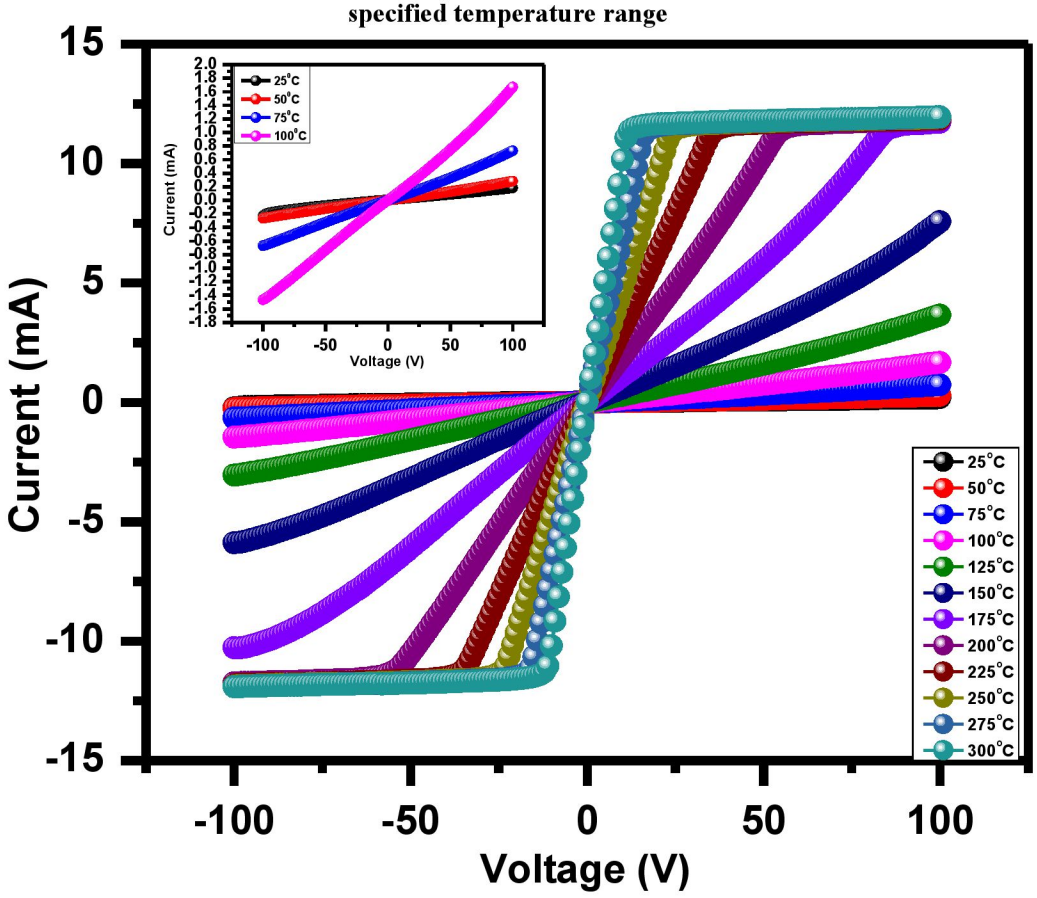


Fig. 9: Variation of leakage current with applied voltage at specific range of temperature for the investigated sillenite sample

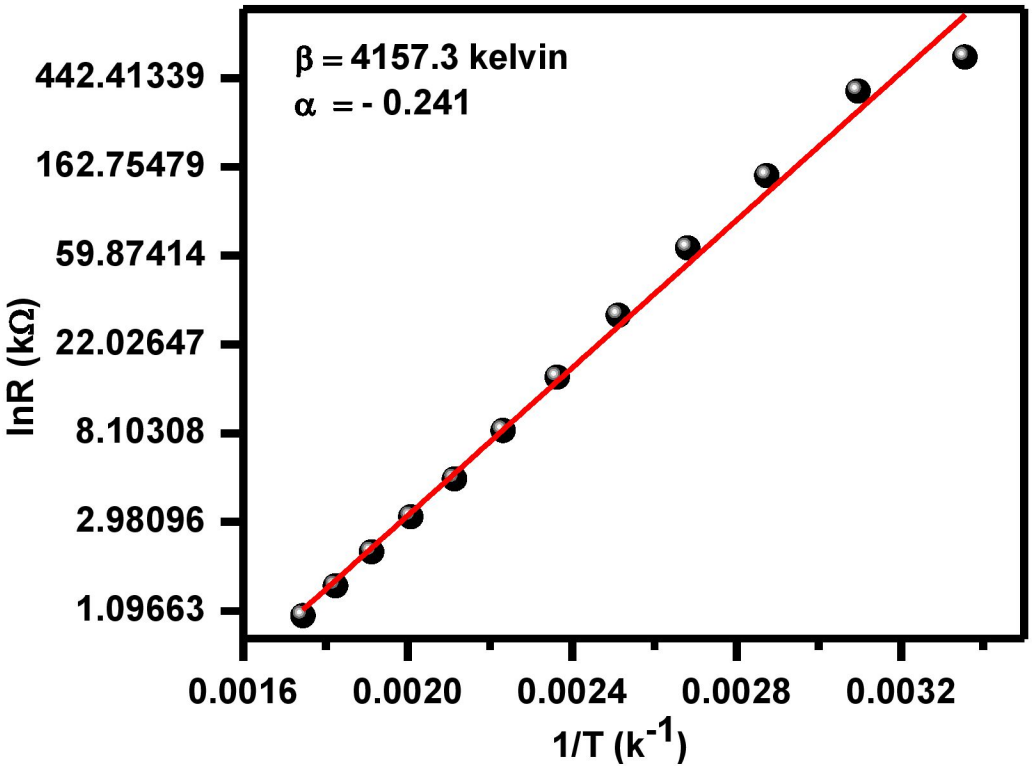


Fig. 10: Variation of resistance of investigated sillenite material with temperature.

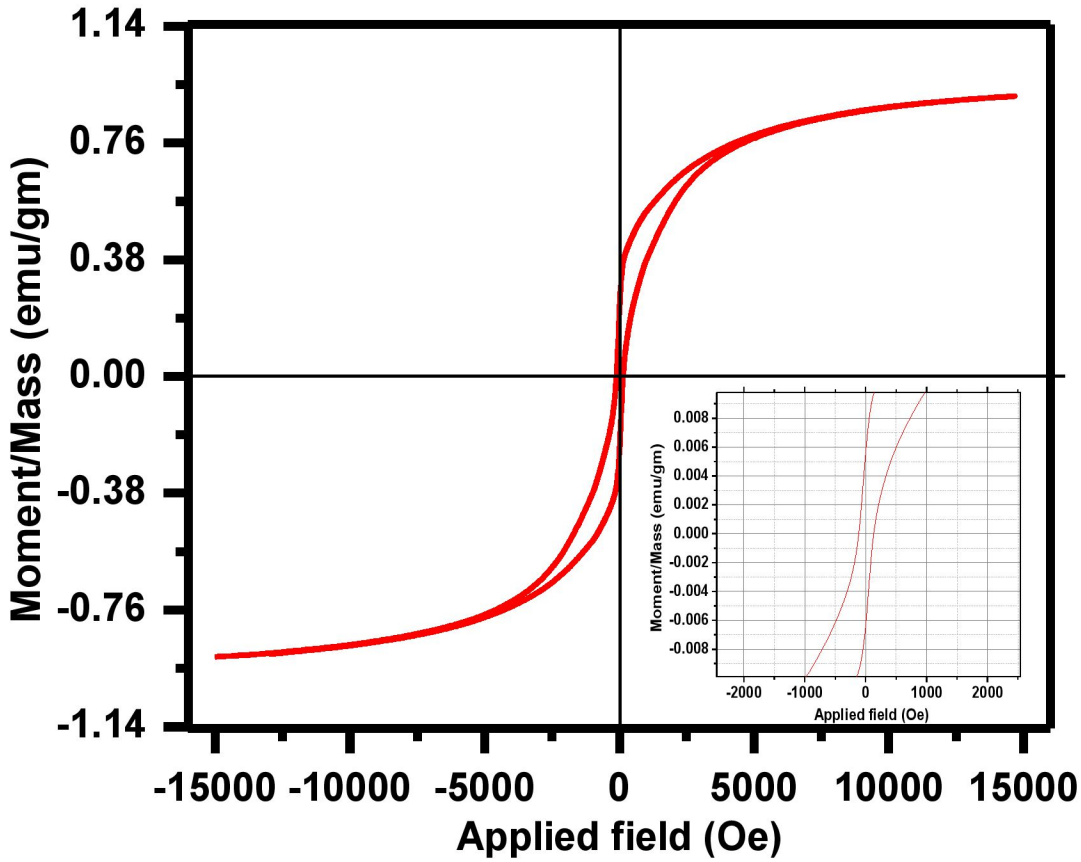


Fig. 11: Variation of magnetization with applied field for the investigated Sillenite sample.

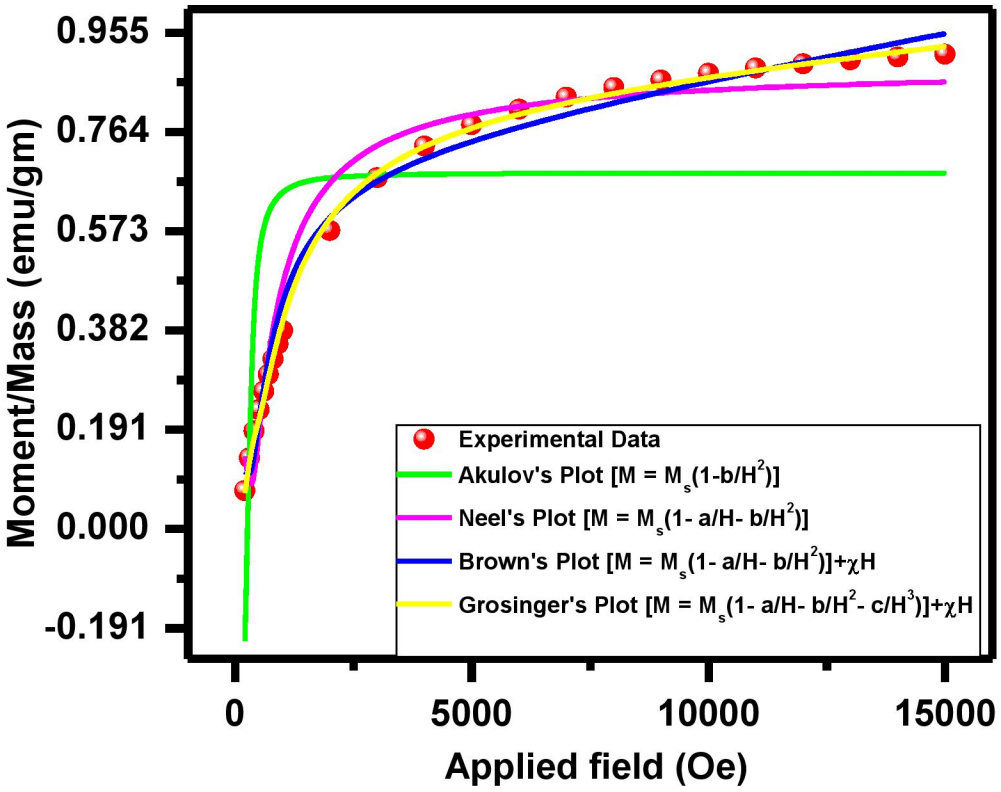


Fig. 12: LAS fitting on the investigated magnetic spectra of studied Sillenite sample

Supplementary Files

This is a list of supplementary files associated with this preprint. Click to download.

- Tablefile.docx